Biosensors and Bioelectronics 142 (2019) 111502

Contents lists available at ScienceDirect

Biosensors and Bioelectronics

journal homepage: www.elsevier.com/locate/bios

Novel electrochemical biosensor for serotonin detection based on gold nanorattles decorated reduced graphene oxide in biological fluids and *in vitro* model

Kuldeep Mahato[a], Buddhadev Purohit[a], Keshav Bhardwaj[b], Amit Jaiswal[b], Pranjal Chandra[a,*]

[a] Laboratory of Bio-Physio Sensors and Nano-bioengineering, Department of Biosciences and Bioengineering, Indian Institute of Technology Guwahati, Guwahati, 781039, India

[b] School of Basic Sciences, Indian Institute of Technology Mandi, Mandi, 175005, Himachal Pradesh, India

ARTICLE INFO

Keywords:
Serotonin
Electrochemical biosensor
Label-free
Clinical determination
Au-nanorattles
In vitro detection

ABSTRACT:

Abnormal level of serotonin (ST) in body fluids is related to various clinical conditions including behavioral and psychotic disorders; hence its fast detection in clinically relevant ranges have tremendous importance in medical science. In view of this, we have developed a novel biosensor for ST detection using Au-nanorattles (AuNRTs)-reduced graphene oxide (rGO) nanocomposite coated on to the gold nanoparticles (AuNPs) deposited glassy carbon electrode (GCE). The nanocomposite/sensor probe was characterized using UV–Vis, TEM, SAED, EDX, AFM, and electrochemical techniques including LSV and EIS. Thereafter, the suitability of fabricated GCE/AuNPs/AuNRTs-rGO-Naf sensor probe was applied for ST determination which showed a linear dynamic range (LDR) of 3×10^{-6} - 1×10^{-3} M and the detection limit (DL) of 3.87 (± 0.02) $\times 10^{-7}$ (RSD < 4.2%) M, which falls in the ranges of normal as well as various abnormal pathophysiological conditions. The designed sensor is successfully applied to detect ST in various real matrices *viz.* urine, blood serum, and *in vitro* model to show its direct clinical/practical applicability. Interferences due to the coexisting molecules were assessed and the long-term stability of the designed sensor was also examined which was found to be 8 weeks.

1. Introduction

Serotonin is one of the principle neurotransmitter (NTs), chemically known as 5-hydroxytryptamine and is regarded as molecule of contentment as it participates actively in controlling a number of behavioral as well as cognitive activities (Godoy-Reyes et al., 2018). It is majorly produced by the brain under physiological conditions, where it functions in passing the information to various organs through the central nervous system (Lacasse and Leo, 2005). In addition, the gastrointestinal tract has also been reported for secreting ST to control the intestinal movement (Camilleri, 2009). Its abnormal levels have been related not only with various disorders *viz.* neurodegenerative diseases, autism, inflammatory syndromes, but also linked with a number of psychotic states including; attention-deficit hyperactivity disorder (Carver et al., 2009). Its abnormally high serum level is associated in various carcinoid tumors, commonly arising from the gastrointestinal tract. Thus, ST determination in bio-fluids *viz.* serum and urine level have become one of the confirmatory tests for carcinoid tumors in clinics (Feldman, 1986; Godoy-Reyes et al., 2018). The serum serotonin level in carcinoids have been reported > 400 ng/mL (*i.e.* 22.59×10^{-7} M) in case of tumorigenic growth, while further elevated level > 1000 ng/mL (*i.e.* 56.74×10^{-7} M) was reported in metastatic state. This is much higher than the normal clinical serum level of ST, which is up to 300 ng/mL (*i.e.* 17.01×10^{-7} M) (Plapp, 2019).

In clinical tests for the confirmation of such severity, ST has been determined in various samples using the conventional methods majorly based on the fluorimeter (Andén and Magnusson, 1967), capillary electrophoresis (Šolínová et al.,2019), high-performance liquid chromatography (Patel et al., 2005), enzyme-based immunoassay (Maurer-Spurej et al., 2002), chemi-luminescence (Barnett et al., 1998), and mass spectrometry (Yılmaz et al., 2019). These methods are powerful and sensitive, but involves tedious processes, sophisticated high-end instruments, longer time, and are often required the sample pretreatment before testing, which not only restricts their utility for real time implications but also limits their usage in onsite point-of-care analyses. In order to address these issues, a number of advanced strategies have also been employed; where electrochemical biosensor based systems have found great attention due to their high sensitivity, ultrafast

* Corresponding author.
E-mail address: pchandra13@iitg.ac.in (P. Chandra).

https://doi.org/10.1016/j.bios.2019.111502
Received 30 April 2019; Received in revised form 26 June 2019; Accepted 12 July 2019
Available online 13 July 2019
0956-5663/

detection, and miniaturizability (Baranwal and Chandra, 2018; Moon et al., 2018). Despite the advancement in the developed electrochemical ST determination, they suffer because of interfering signals due to the presence of inherently coexistent molecules and NTs *viz.* ascorbic acid, dopamine, epinephrine, norepinephrine etc. due to their close reduction potentials (Wu et al., 2003), which not only make the systems insensitive but also non-selective. Therefore, in order to eliminate such limiting factors, the nanomaterial-empowered strategies were employed, where nanomaterials were introduced to achieve better-resolved determination of NTs by tuning the effective reduction potentials (Baranwal and Chandra, 2018). In this context, a number techniques were employed by exploiting their intrinsic optoelectronic properties in nano-domain including a wide range of metallic and composites *viz.* metal oxides, polymers, and carbon based nanocomposites (Durairaj et al., 2018; Si and Song, 2018). Recently, caged-nanostructures, particularly nanocages and nanorattles have found wide attention for various application including, adsorbent, drug delivery agent, nanoreactor etc. due to their extremely high surface area, porosity, and unique properties (Ahlawat et al., 2019; Priebe and Fromm, 2015; Singh et al., 2018).

Since, ST biosensor relies on its electro-catalysis at probe surface, conducting nature of the constituents probe materials, and electroactive surface area play a crucial role (Yang et al., 2015; Zestos, 2018). Thus, nanorattles-based composites could serve a promising material for the sensor probe fabrication. In our previous study, we have discussed that nanorattles possess three available surfaces *i.e.* (i) the outer porous shell, (ii) the inner wall of the cubic shell, and (iii) the surface of inner solid core (Singh et al.,2017, 2018; Ahlawat et al., 2019). This unique structure not only provide larger surface area for catalysis and electrocatalysis, but it may also assist selective channelization of redox active small molecules (e.g. ST) through its porous cage to the solid core by restricting the bulky coexisting entities (e.g. proteins, lipids etc.) present in biological samples. These bulky groups often reported to foul the electrode surface and thus sensitivity is compromised in real sample analyses. Therefore, nanorattles based composites could be a promising and important probe materials for ST biosensor design and application in various biological matrices.

In the present study, we have developed a novel nanocomposite comprising AuNRTs - rGO, which was coated onto the AuNPs deposited GCE for the label-free detection of ST. The sensor material/probe was characterized by UV–Visible spectroscopy (UV–Vis), transmission electron microscopy (TEM), selected area electron diffraction (SAED), energy dispersive X-ray photoelectron spectroscopy (EDX), atomic force microscopy (AFM), linear sweep voltammetry (LSV), and electrochemical impedance spectroscopy (EIS). Further, the probe was used for the determination of ST in standard conditions, where the dose dependent study was performed and analytical performances were obtained using differential pulse voltammetry (DPV). The practical implications of the probe were examined in serum, urine, and *in vitro* cell samples using spike and recovery method. The selectivity test for the fabricated probe towards ST was assessed and the shelf-life of the developed biosensor was also evaluated.

2. Experimental

2.1. Chemicals and instruments

All the chemicals and instruments used have been described in the supplementary information (SI-1).

2.2. Synthesis of AuNRTs

AuNRTs have been synthesized using seed mediated process shown in Scheme 1(A). The detailed procedure has been discussed in supplementary information (SI-2).

2.3. AuNRTs-rGO-Naf nanocomposite preparation and fabrication of GCE/AuNPs/AuNRTs-rGO-Naf sensor probe

The AuNRTs-rGO-Naf nanocomposite was prepared by doping AuNRTs in rGO containing Naf (0.1% in alcohol). In the first step, the AuNRTs were extracted in ethanol, where 1 ml of the previously synthesized aqueous solution was centrifuged at 8000 rpm for 10 minutes and were re-suspended in 1 mL of ethanol. In the meantime, rGO solution was obtained by dissolving the rGO (10 mg/mL) in ethanol separately. Thereafter, these separately prepared solutions were mixed in the ratio of 1:5 (v/v) (optimized), which also contains 0.1% nafion. The solution was then sonicated for 4 hours in order to obtain AuNRTs-rGO-Naf nanocomposite which was used to develop the sensor probe. Further, GCE electrode was polished with 0.05 μm alumna slurry on a microcloth pad and was rinsed with deionized water. After this, AuNPs were electro-chemically deposited onto the GCE using a potential step method in an acidic solution (0.5 M H_2SO_4) containing 0.0025% $HAuCl_4$ by performing LSV between +1.5 and + 0.4 (V) *vs.* Ag/AgCl. The AuNPs electrodeposition conditions are as follows: 60.0 s deposition time, − 0.6 V deposition potential, 0.1 V s^{-1} scan rate with five sweeps. Thereafter, the AuNRTs-rGO-Naf nanocomposite (2 μL) was coated onto the GCE/AuNPs surface. The final probe was termed as GCE/AuNPs/AuNRTs-rGO-Naf. The detailed process of GCE/AuNPs/AuNRTs-rGO-Naf sensing probe fabrication is shown in Scheme 1.

2.4. Mammalian cell culture and human serum sample preparation

Mammalian cell culture and human serum sample were prepared using standard method. Details processes have been discussed in SI-3.

3. Results and discussions

3.1. Characterization of the AuNRTs-rGO nanocomposite

The AuNRTs-rGO nanocomposite have been characterized using UV–Vis, FESEM, HR-TEM, and SAED. In, UV–Vis spectrum (Fig. 1(A) (i); blue curve), a absorbance peak at 657 nm (λ_{max}) was observed in case of AuNRTs due to the SPR arising from its porous shell structure (Singh et al., 2017). In addition, a shoulder at around 540 nm is contributed by the inner solid octahedron core present inside the cubic porous shell (Singh et al., 2017). The peak at 657 nm was reconfirmed by performing a dose dependent UV–Vis analyses, where gradual increase in the absorbance at 657 nm was observed with increasing AuNRTs concentrations (Fig. 1(B)). A dose dependent plot was obtained using the UV–Vis responses (inset Fig. 1(B)), which shows linear increment of peaks at λ_{max} (657 nm) indicating this peak is merely due to the AuNRTs. In the UV–Vis spectrum corresponding to rGO (Fig. 1(A) (ii); red), an absorption peak near λ_{max} (260 nm) was observed due to the optical absorption of π-π* transition of aromatic C═C, C═O, and C–O bonds. Interestingly, in the UV-Vis spectrum of nanocomposite comprising AuNRTs and rGO (Fig. 1(A) (iii); gray) two clear peaks near the 260 and 660 nm appeared which were observed separately when these materials were tested individually. These results clearly indicate the formation of AuNRTs-rGO nanocomposite.

Further, in order to validate AuNRTs-rGO nanocomposite formation, we have characterized it by TEM. Fig. 1(C) shows the representative TEM micrograph of the nanocomposite, where it is evident that AuNRTs (black squares) are present not only on the surface of rGO sheets, but also found entrapped within the multi-folded rGO layers, indicating the successful formation of the nanocomposite. The size distribution of the particles was evaluated where the average size was found to be 45.50 (± 1.25) nm (Fig. 1(C) inset). To study the crystal structures, we have further characterized the nanocomposite using HR-TEM and SAED. The representative HR-TEM micrograph and SAED pattern are shown in Fig. 1(D)–(E), respectively. From the HR-TEM micrograph, it is evident that the synthesized AuNRTs are of crystalline

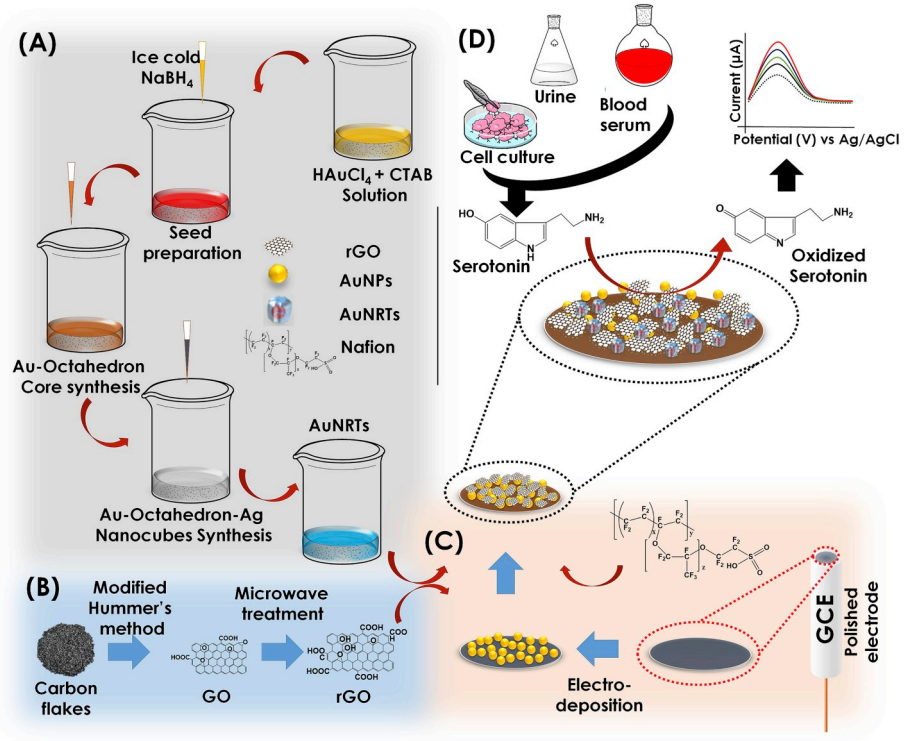

Scheme 1. Schematic representation for the synthesis/deposition of AuNRTs (A), rGO (B), and AuNPs (C) on the GCE; the sensor probe development using AuNRTs-rGO-Naf nanocomposite and ST detection mechanism (D).

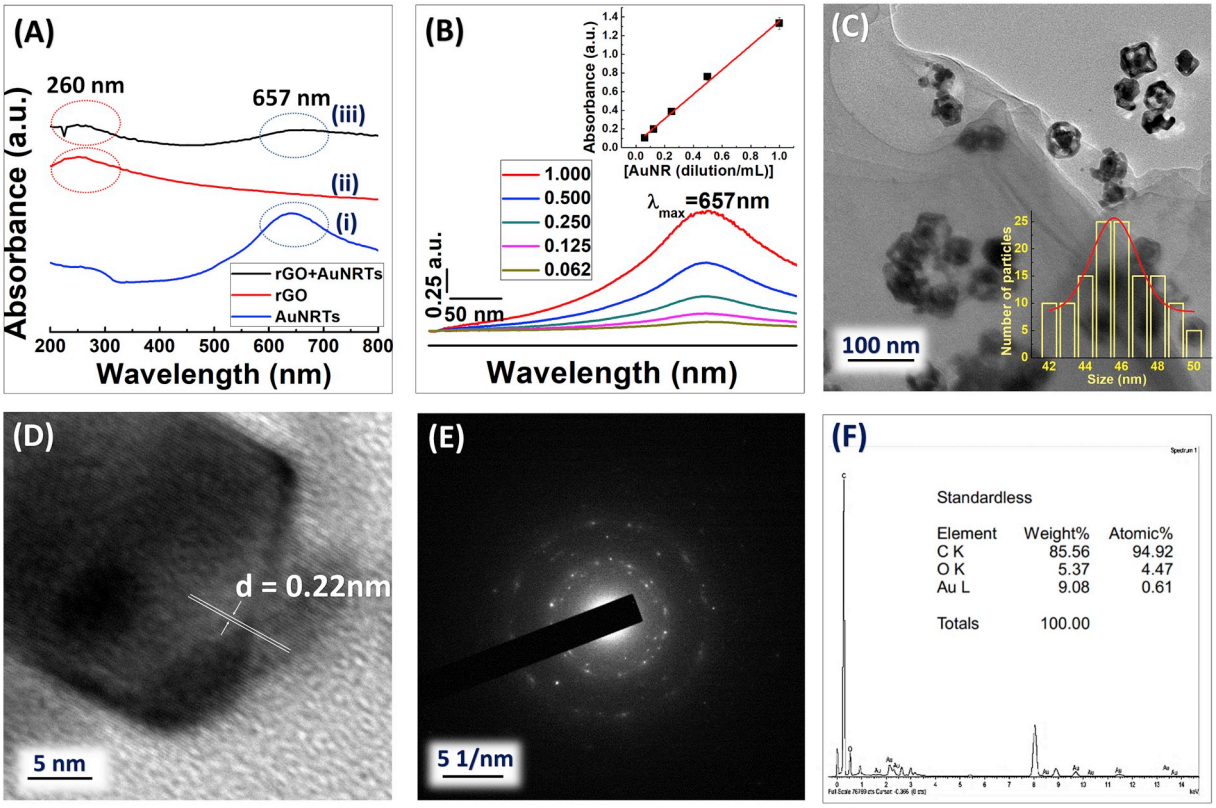

Fig. 1. Physical characterization of AuNRTs-rGO nanocomposite; (A) UV–Visible spectra of (i) AuNRTs, (ii) rGO, and (iii) AuNRTs-rGO; (B) dose dependent responses of the AuNRTs (inset: calibration plot); (C) representative TEM micrographs of AuNRTs-rGO composite (inset: particle size distribution plot); (D) HR-TEM micrograph and d-fringe of the AuNRTs; (E) SAED pattern of AuNRTs-rGO nanocomposite; (F) EDX of the AuNRTs-rGO nanocomposite.

in nature with the inter-planer distances $d = 0.22$ nm, which is due to the presence of gold in AuNRTs. The SAED image shows the multiple concentric rings around central maxima indicating the polycrystalline nature of the nanocomposite, which is comprised of two highly crystalline components *viz.* AuNRTs and rGO. Further, to validate the elemental composition of the nanocomposites, we have complimented the characterization by using EDX and observed the elemental composition of C, O, and Au with the weight percentage of 85, 5, and 9%, respectively (Fig. 1(F)), indicating the nanocomposite have no other impurities.

3.2. Characterization of GCE/AuNPs/AuNRTs-rGO-Naf sensor probe

Using the synthesized AuNRTs-rGO nanocomposite a sensor probe was fabricated as described in Scheme 1. In order to evaluate the electron transfer properties, the fabricated sensor probe has been characterized extensively using the electrochemical methods. Firstly, the formation of AuNPs was characterized by LSV, where a clear reduction peak at 0.95 (V) vs. Ag/AgCl was observed, which was due to the reduction of Au^{3+} to Au^0 on the electrode surface, forming AuNPs. Interestingly, the peak current at 0.95 V increased with five consecutive LSV sweeps, indicating the formation of a highly conducting electrode surface due to the further deposition of AuNPs (Figure SI-1). In the next step, the sensor probe was dipped into the electrochemical cell containing 5 mM ruthenium hexamine (RuHex) prepared in PBS. In this step, all modified surfaces were evaluated using LSV technique and anodic peak current responses were recorded at the potential window of −0.75 to 0.4 V at the scan rate of 50 mV/s. Fig. 2(A) shows the representative LSVs at bare GCE (black), GCE/AuNPs (red), GCE/AuNRTs-Naf (blue), GCE/rGO-Naf (pink), GCE/AuNPs/AuNRTs-Naf (gray), and GCE/AuNPs/AuNRTs-rGO-Naf (yellow). The current response due to RuHex at GCE/AuNPs was found to be higher compared to the bare GCE due to the enhanced conductivity and surface area. The similar increment in the current has also been observed at the GCE/AuNRTs-Naf surface, indicating the conducting nature of the AuNRTs and its capability of assisting electrochemical signal. In the next surface, we have replaced AuNRTs with rGO and the response of the GCE/rGO-Naf surface was recorded in similar experimental conditions. The subtle increment of the current, in this case was also observed in the LSV responses. Next, we tested GCE/AuNPs/AuNRTs-Naf electrode, where higher current was observed in LSV than the previously tested surfaces. Intriguing by these interesting results, we developed the GCE/AuNPs/AuNRTs-rGO-Naf sensor probe. It is interesting to note that, in this case, the highest current was observed due to the synergistic behavior of AuNRTs and rGO present in the sensing matrix. Therefore, for the further analyses, we have used the GCE/AuNPs/AuNRTs-rGO-Naf as a sensor probe. In order to evaluate the importance of modified electrode surfaces towards electrochemical sensing, we have calculated the diffusion coefficients of bare GCE and for each layer of the modified electrode using Randles-Sevcik's model (equation (1)).

$$I_p = (2.69 \times 10^5) n^{3/2} A C D^{1/2} v^{1/2} \quad (1)$$

Where I_p is the peak current (in ampere), n is the number of electron transferred in redox process (here n = 1), A is the electrode surface area (in cm^2: here A = 0.01 cm^2), C is the concentration of electroactive species (in mole cm^{-3}), D is the diffusion coefficient (in cm^2/s), and v is the scan rate (in V/s).

The diffusion coefficient (*D*) values for bare GCE, GCE/AuNPs, GCE/AuNRTs-Naf, GCE/rGO-Naf, GCE/AuNPs/AuNRTs-Naf, and GCE/AuNPs/AuNRTs-rGO-Naf modified surfaces were found to be 2.19×10^{-4}, 2.42×10^{-4}, 2.51×10^{-4}, 2.80×10^{-4}, 3.05×10^{-4}, and 5.40×10^{-3} cm^2/s, respectively. The findings of Randles - Sevcik model clearly indicates the ~2.5 fold higher transfer of charged species through the GCE/AuNPs/AuNRTs-rGO-Naf modified electrode surface than the bare GCE. These results were also validated using the EIS, where spectra in the Nyquist plots were recorded to obtain the charge transfer resistance (R_{ct}) values (Fig. 2 B). The R_{ct} values obtained were 1307.26 (± 45.75)Ω, 1257.12 (± 43.99)Ω, 1131.42 (± 39.59)Ω, 1057.2 (± 37.00)Ω, 992.98(± 34.75)Ω, and 174.72(± 10.11)Ω for the bare GCE, GCE/AuNPs, GCE/AuNRTs-Naf, GCE/rGO-Naf, GCE/AuNPs/AuNRTs-Naf, and GCE/AuNPs/AuNRTs-rGO-Naf surfaces, respectively (Fig. 2(C)). It is interesting to note that the lowest R_{ct} was obtained for GCE/AuNPs/AuNRTs-rGO-Naf surface compared to other tested surfaces. This was due to the fastest electron transfer process at the electrode/electrolyte interface in this case. The charge transfer is a crucial parameter for the modified surfaces due to its complexity. In order to investigate the charge transfer behavior and stability of modified electrode surfaces for electrochemical analysis, we have further performed scan rate studies at bare GCE, GCE/AuNPs, GCE/AuNRTs-Naf, GCE/rGO-Naf, GCE/AuNPs/AuNRTs-Naf (Figure SI-2), and GCE/AuNPs/AuNRTs-rGO-Naf (Fig. 2(D)). Here, LSV responses were recorded between 10 and 100 mV/s in 5 mM RuHex prepared in PBS. The peak currents were found to be directly proportional to the square root of scan rates in all the cases with the correlation coefficient between 0.997 and 0.999, indicating the diffusion-controlled charge transfer process. These results confirm that the developed GCE/AuNPs/AuNRTs-rGO-Naf probe is highly stable, conducting, and sensitive; hence, it is suitable for electrochemical analysis.

Thereafter, in order to confirm the macroscopic changes at the modified electrode surface, each layer was characterized using AFM. Fig. 2(E) and Figure SI-3 shows AFM micrographs and *z-deflections* profile of the surfaces at different stages of fabrication, respectively *i.e.* bare electrode (i), AuNPs deposited electrode (ii), and AuNRTs-rGO-Naf coated electrode (iii). At first, the surface topology of bare electrode was captured which shows the smooth morphology. The mean surface roughness and *z-deflection* were obtained to be 0.50 nm and 3 nm, respectively. The AuNPs deposited surface shows a granular morphology with the mean surface roughness and *z-deflection* of the 4.81 nm and 11 nm, respectively; indicating the successful AuNPs deposition. In the final surface, a more dense film-like morphology was observed with the mean surface roughness and *z-deflection* of 7.90 nm and 26 nm, respectively, indicating the successful coating of AuNRTs - rGO over the electrode surface.

3.3. Analytical performance of the GCE/AuNPs/AuNRT-rGO-Naf sensor probe

After the successful characterization, the GCE/AuNPs/AuNRTs-rGO-Naf sensor probe was applied for the detection of ST. At first, we have tested the suitability of the fabricated probe for ST detection. For that, bare GCE was dipped in 5 mM PBS (Blank/no ST) and LSV was recorded by sweeping the potentials between 0.25V and 0.55V, where no peak was observed. In the subsequent step, the LSV response was recorded in 5 mM PBS containing 10^{-4} M ST using bare GCE probe, where a broad peak at 0.39V was observed, which is due to the presence of ST in an electrolyte solution. Next, the GCE/AuNPs/AuNRTs-rGO-Naf sensor probe was tested in the same solution and LSV was recorded in the similar potential window. Interestingly, a sharp amplified peak at a relatively lower potential 0.37 V was observed, which is due to the electro-catalytic activity of the sensor probe towards ST. The signal response in this case was two-fold higher compare to the bare GCE at the same concentration of ST (*i.e.*10^{-4} M), indicating the fabricated sensor is capable of sensitive ST detection (Fig. 3(A)). In order to validate that the peak observed at 0.37 V was merely due to the interaction of ST with sensor probe, we performed two separate control experiments. In first experiment, a concentration dependent study was performed, where we tested 1×10^{-5}, 3×10^{-5}, 6×10^{-5}, and 1×10^{-4} M of ST. Fig. 3(B) shows the signal responses, where peak currents increased linearly with increasing ST concentrations. The representative dose dependent LSV responses are shown in inset of Fig. 3(B). The linear regression equation for concentration dependent

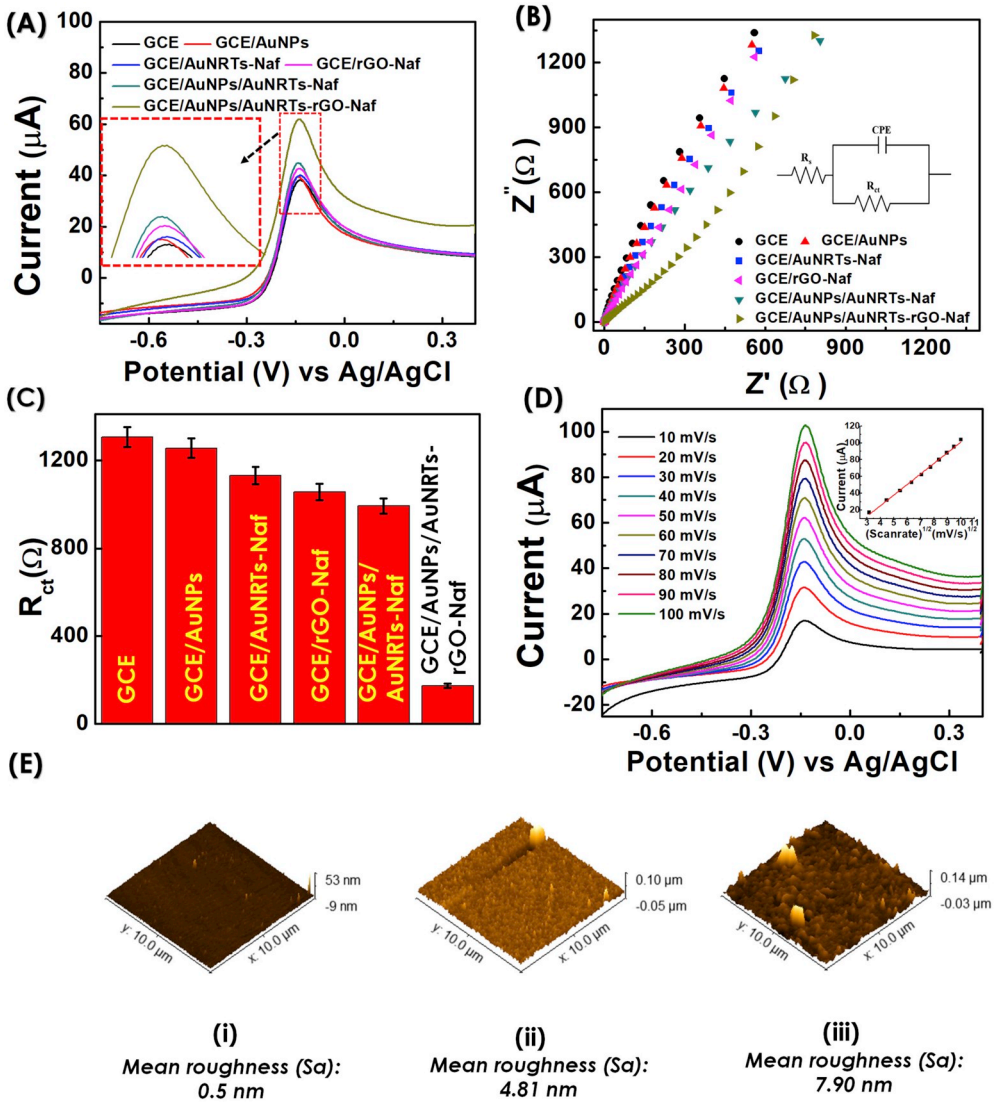

Fig. 2. LSV (A) and EIS (B) responses of bare GCE, GCE/AuNPs, GCE/AuNRTs-Naf, GCE/rGO-Naf, GCE/AuNPs/AuNRTs-Naf, GCE/AuNPs/AuNRTs-rGO-Naf modified electrode surfaces; (C) histograms showing the respective R_{ct} values obtained from the EIS spectra; (D) LSV responses of the GCE/AuNPs/AuNRTs-rGO-Naf modified surfaces at different scan rates (10–100 mV/s); (E) AFM micrograph of the bare electrode surface (i), AuNPs deposited electrode surface (ii), and AuNRTs-rGO-Naf deposited electrode surface (iii) with *z-deflection* and respective mean surface roughness.

plot is expressed as follows: $\Delta I(\mu A) = 14.87 \times 10^{-6} (\pm 0.61 \times 10^{-6}) + 2.18 \times 10^{-6} (\pm 0.13 \times 10^{-6})$Log conc [ST(M)] with the correlation coefficient of 0.96, indicating the ability of GCE/AuNPs/AuNRTs-rGO-Naf sensor probe for ST detection correctly. In the second control experiment, a scan rate dependent study was performed at 10^{-3} M of ST between 10 and 100 mV/s (Figure SI-4). In this case, the peak current was directly proportional to the square root of scan rates due to the diffusion controlled electrochemical process of ST only. The results obtained from both the control experiments validate that the designed sensor probe is stable and is able to detect ST accurately. Comparable peak potential for ST detection has also been reported at GCE/MWCNT-NiO electrode (Fayemi et al., 2017). Further, we investigated the analytical performance of GCE/AuNPs/AuNRTs-rGO-Naf sensor by detecting various concentrations of ST using DPV.

Firstly, the multiple blanks have been recorded in DPV using GCE/AuNPs/AuNRTs-rGO-Naf, where no foreign peaks or deflections were observed under the operational potential window (inset of Fig. 3(C)). Thereafter, the dose dependent ST analysis was performed using GCE/AuNPs/AuNRTs-rGO-Naf sensor. Fig. 3(C) shows the representative DPV curves, where the current response increased linearly with the increase in the ST concentrations. Based on the DPV responses a calibration plot was obtained, which shows the LDR between 3×10^{-6} and 1×10^{-3} M of ST (Fig. 3(D)). The linear regression equation of the calibration plot for ST detection was expressed as follows: $\Delta I (\mu A) = 3.80 \times 10^{-6} (\pm 0.38 \times 10^{-6})$ Log conc [ST(M)] + $20.41 \times 10^{-6} (\pm 1.66 \times 10^{-6})$ with the correlation coefficient of 0.95. The DL, in this case was determined to be $3.87 (\pm 0.02) \times 10^{-7}$ M (RSD < 4.2%,95% confidence level, n = 3) using equation (2). It is worth mentioning that the detection range in our case falls well in the clinical range related to various pathophysiological conditions including carcinoid syndromes/tumors (Feldman, 1986; Plapp, 2019) and pre-eclampsia (Vural et al., 1999).

$$LOD = \frac{3SD_B}{Slope} = \frac{3SD_B}{\frac{dy}{dx}} = \frac{3SD_B}{\frac{dy}{d\ln x} \times \frac{d\ln x}{dx}} = \frac{3SD_B}{\frac{dy}{2.303(d\log x)} \times \frac{1}{x}}$$

$$= \frac{3(2.303)SD_B x}{\frac{dy}{(d\log x)}} = \frac{3(2.303)SD_B x}{\text{slope of the semilog plot}} \quad (2)$$

Where, SD_B is standard deviation of blank; x is the limit of quantification or lowest concentration measured.

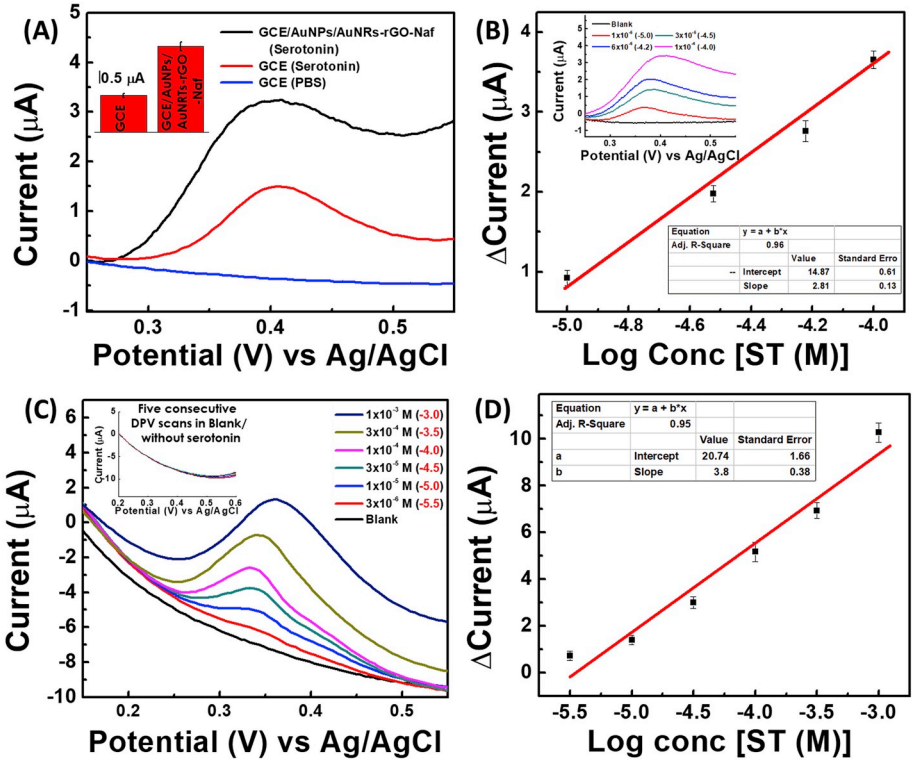

Fig. 3. (A) LSV responses at bare GCE and GCE/AuNPs/AuNRTs-rGO-Naf in absence/presence of ST; (B) dose dependent plot obtained for ST analysis at different concentrations between $1 \times 10^{-5}$and 1×10^{-4} M) by using the sensor probe, (inset shows corresponding LSV responses); (C) DPV responses of the sensor probe at various concentrations of ST between 3×10^{-6} and 1×10^{-3} M, (inset shows DPV responses of sensor probe in blank PBS/without ST; five consecutive scans); (D) the corresponding calibration plot obtained from the dose dependent DPV responses.

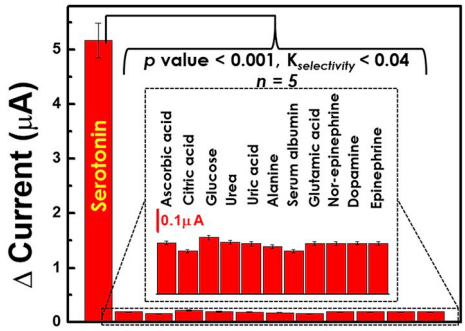

Fig. 4. Selectivity assay of GCE/AuNPs/AuNRTs-rGO-Naf sensor probe.

3.4. Selectivity assay

Another most critical parameter to assess the biomedical values of developed sensors is selectivity (Mahato and Chandra, 2018; Mahato et al., 2018; Pallela et al., 2016). For that, the GCE/AuNPs/AuNRTs-rGO-Naf sensor was tested towards ascorbic acid (10 mg/mL) due to its coexistence in higher concentrations and close reduction potential to ST in the biological samples. Not only this, we have also tested citric acid (1 mg/mL), uric acid (1 mg/mL), glutamic acid (1 mg/mL), glucose (10 mg/mL), serum albumin (1 mg/mL), urea (1 mg/mL), and alanine (1 mg/mL), which are the most common biochemicals present in the real sample matrices. These molecules are present in μg/mL in normal conditions (Burtis et al., 2012), but we have tested them at 10^3 times higher concentrations to show the accuracy of our sensor probe. No signal was obtained for alanine, ascorbic acid, citric acid, uric acid, and glutamic acid most likely due to the precise operational potential window and/or their repulsion from the negatively charged electrode surface. In case of glucose, serum albumin, and urea, no peaks were obtained due to their electrochemical inertness and/or inability of the sensor probe material to electro-catalyze them. Other NTs *viz.* dopamine, epinephrine, and nor-epinephrine are profoundly reported in coexistence with ST, hence the interference due to them may be possible. Therefore, we have tested the sensor probe for these NTs at 1 mg/mL, where no current responses were observed at 0.37V, however, the peaks for these NTs were observed at 0.25 V. These results clearly indicate that these NTs do not interfere towards ST detection. The selectivity of the sensor probe was mathematically deduced by determining the selectivity coefficient $K_{selectivity}$using equation (3).

$$K_{selectivity} = \frac{(Signal)_{interferent}}{(Signal)_{ST}} \quad 3$$

Where $K_{selectivity}$ is the coefficient of selectivity, $(Signal)_{interferent}$is the signal due to the interfering molecules, and $(Signal)_{ST}$is the signal corresponds to ST.

The calculated $K_{selectivity}$ values for tested molecules were found to be extremely low ($k_{selectivity}$«1), indicating that the fabricated sensor is highly selective towards ST. We also performed T-test and calculated *p-values* against all the tested molecules, which were found to be «0.001 (n = 5), indicating that the selectivity results are statistically significant. Fig. 4 shows the histogram obtained from DPV responses of the interfering molecules and ST at the GCE/AuNPs/AuNRTs-rGO-Naf sensor probe.

3.5. Real sample analysis

There are number of pathophysiological conditions, where the variable levels of ST in urine, blood, and cellular systems have been reported (Feldman, 1986; Murugesan et al., 2018). Therefore, these matrices were selected for real sample analyses using spike and recovery method. Firstly, various concentrations of ST was detected in PBS equilibrated urine samples using the GCE/AuNPs/AuNRTs-rGO-Naf sensor probe. It is worth mentioning that the urine samples were not subjected to any pretreatment step such as filtration or centrifugation before processing. The results of these experiments were analyzed and % recoveries of ST were calculated using equation (4).

$$\%\text{Recovery} = \frac{([S]_{ST} - [B]_{ST})}{[SS]_{ST}} \quad 4$$

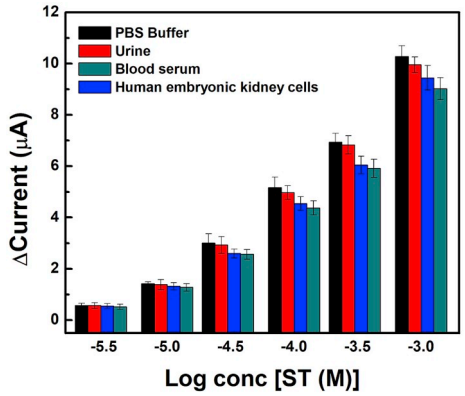

Fig. 5. Comparative concentration dependent determination of ST in PBS (black bars) urine (red bars), blood serum (gray bars), and *in vitro* model (blue bars). (For interpretation of the references to colour in this figure legend, the reader is referred to the Web version of this article.)

Where, $[S]_{ST}$ *and* $[B]_{ST}$ *are the analytical responses of* ST *in the spiked and blank urine samples, respectively; and* $[SS]_{ST}$*is the analytical response of* ST *in the standard solutions.*

Fig. 5 shows the signal response of ST detected in urine samples (red bars), where peak currents increased linearly with the increase in ST concentrations from 3×10^{-6} to 1×10^{-3}M. The sensitivity of ST detection was evaluated by comparing the DPV signals obtained from urine samples with blank buffer (black bars). Interestingly, the designed biosensor is able to detect 96.23–98.49% of ST from the human urine samples. Based on the dose dependent ST detection in urine, a calibration plot was obtained which shows the linear regression equation as follows: $\Delta I(\mu A) = 3.71(\pm 0.33)\times 10^{-6}$Log conc [ST(M)] + 20.28 $(\pm 1.47)\times 10^{-6}$M with the correlation coefficient of 0.959. The DL of $4.93(\pm 0.32)\times 10^{-7}$M (RSD < 3.58%) was obtained in human urine sample based on the standard deviation of three times consecutive analyses of the blank (95% confidence level; n = 3), which indicates the fabricated biosensor is efficient to detect ST in human urine sample and is highly reproducible. Further, the fabricated probe was challenged for the determination of ST in relatively complex matrices. For this purpose, the fabricated probe was used to detect ST in clinical serum samples. Herein, human blood sample was obtained from IITG hospital and serum was extracted by following the standard protocol. Thereafter, the serum was equilibrated with PBS and used for the determination of ST. Similar to the assessment in urine samples, here also different concentrations (1×10^{-3} to 3×10^{-6}) of the ST were spiked and DPV responses were recorded (Fig. 5; blue bars). Based on the DPV responses, % recovery for ST were calculated, which were found in between 84.62 and 90.69%, indicating the fabricated probe is capable of detecting ST even in the complex matrix like blood serum. Based on the dose dependent responses in serum samples, a calibration plot was traced and the regression equation was obtained as follows: ΔI (μA) = $3.31(\pm 0.34)\times 10^{-6}$ Log conc [ST(M)] + 18.06 $(\pm 1.50)\times 10^{-6}$M with the correlation coefficient of 0.947 and the DL of $8.73(\pm 0.35)\times 10^{-7}$M (RSD < 4.92%). After demonstrating the ability of the sensor probe for ST detection in biological fluids, we enthusiastically extended our investigation towards *in vitro* ST detection. For this purpose, ST was spiked in the cellular environment in the range of 3×10^{-6} to 1×10^{-3} and recovery was calculated as done for the biological fluids indicated above. Fig. 5 (gray bars) shows the dose dependent increment in ST signals when tested in *in vitro* settings. Similar to the above, here also we have obtained a calibration plot after plotting the peak currents of responses against concentrations spiked. The regression equation was obtained as $\Delta I(\mu A) = 3.45(\pm 0.38)\times 10^{-6}$Log conc [ST(M)] + $18.79(\pm 1.66)\times 10^{-6}$M with the correlation coefficient of 0.932. The DL in this case was found to be $7.37(\pm 0.27)\times 10^{-7}$M (RSD < 4.92%), indicating the sensor is capable of detecting ST even in cellular environments. Thereafter, the % recoveries were calculated which was found to be in between 86.19 and 94.88%. It is interesting to note that the DL in all the real sample matrices was slightly higher compared to the standard buffer conditions, indicating the negligible matrix effect and excellent catalytic ability of GCE/AuNPs/AuNRTs-rGO-Naf sensor probe for the sensitive determination of ST. Table 1 summarizes the analytical details for recovered ST concentrations, RSD, and % recovery for all the tested concentrations in urine (A), blood serum (B), and *in vitro* model (C).

3.6. Reproducibility and stability studies

Reproducibility and stability are the other parameters, which decide the commercialization of any such sensors (Chandra, 2016; Chandra et al., 2017; Mahato et al., 2017). In order to test the fabricated GCE/AuNPs/AuNRTs-rGO-Naf sensor for its reproducibility, the current responses were recorded at five separately prepared sensors. The current responses were found to be negligibly altered when same fabrication procedure was followed (RSD < 3.9%), indicating the developed sensor is highly reproducible. The small deviation was most likely due to the minor difference in sensor development and/or due to handling errors. The long-term stability has also been studied for the fabricated GCE/AuNPs/AuNRTs-rGO-Naf sensor probe, where the sensor was found to be stable until 8 weeks. Thereafter, the response decreases with time suggesting the developed sensor is stable up to 8 weeks.

4. Conclusion

We have fabricated a novel biosensor based on the AuNRTs decorated-rGO/AuNPs nanocomposite for label-free detection of ST. The sensor was characterized by UV–Vis, TEM, SAED, EDX, AFM, and electrochemical techniques. In this study, we have experimentally demonstrated for the first time AuNRTs as a sensor matrix component and its importance in fast electron transfer at electrode/electrolyte interface. The sensor shows excellent analytical performance with the wide LDR of 3×10^{-6}M -1x10^{-3}M with the DL of 3.87 $(\pm 0.02)\times 10^{-7}$ (RSD < 4.2%) M, which falls in the concentration range for various diseases where ST levels are monitored. The biosensor is capable of delivering highly selective and sensitive determination of ST in urine, blood serum, and *in vitro* model. The fabricated sensor shows excellent recoveries between 84.62 and 98.40% of ST in real samples, making it

Table 1
Percent recoveries of ST in different biological matrices.

Spiked ST (M)	(A) Urine			(B) Blood serum			(C) Cell culture		
	Recovered ST (M)	RSD	% Recovery	Recovered ST (M)	RSD	% Recovery	Recovered ST (M)	RSD	% Recovery
3.00×10^{-06}	$2.95(\pm 0.19)\times 10^{-06}$	5.75	98.40	$2.72(\pm 0.09)\times 10^{-06}$	4.48	90.69	$2.84(\pm 0.13)\times 10^{-06}$	4.73	94.88
1.00×10^{-05}	$0.97(\pm 0.06)\times 10^{-05}$	4.14	97.41	$0.89(\pm 0.05)\times 10^{-05}$	3.98	89.53	$0.93(\pm 0.44)\times 10^{-05}$	5.19	93.23
3.00×10^{-05}	$2.92(\pm 0.17)\times 10^{-05}$	5.97	97.37	$2.55(\pm 0.13)\times 10^{-05}$	4.52	85.07	$2.58(\pm 0.12)\times 10^{-05}$	4.78	86.19
1.00×10^{-04}	$0.96(\pm 0.05)\times 10^{-04}$	5.33	96.23	$0.84(\pm 0.03)\times 10^{-04}$	3.78	84.62	$0.87(\pm 0.41)\times 10^{-04}$	3.72	87.82
3.00×10^{-04}	$2.95(\pm 0.14)\times 10^{-04}$	4.86	98.49	$2.55(\pm 0.17)\times 10^{-04}$	5.58	85.22	$2.61(\pm 0.01)\times 10^{-04}$	4.68	87.15
1.00×10^{-03}	$0.96(\pm 0.03)\times 10^{-03}$	3.59	96.8	$0.87(\pm 0.04)\times 10^{-03}$	4.76	87.79	$0.91(\pm 0.04)\times 10^{-03}$	5.12	91.86

suitable for various clinical applications. The biosensor shows high selectivity towards ST and was found stable up to 8 weeks. The fabricated biosensor has many remarkable features including ease to handle, fast, label-free, and inexpensive detection; thus, it could be a method of choice for ST determination in the biological and clinical samples obtained from hospitals. In the future, the developed biosensing system can be translated towards a genuine miniaturized sensing device for various applications.

Declaration of interest

The authors declare that they have no known competing financial interests or personal relationships that could have appeared to influence the work reported in this paper.

CRediT authorship contribution statement

Kuldeep Mahato: Conceptualization, Data curation, Formal analysis, Investigation, Methodology, Validation, Visualization, Writing - original draft, Writing - review & editing. **Buddhadev Purohit:** Data curation, Formal analysis, Investigation, Methodology, Validation, Writing - original draft, Writing - review & editing. **Keshav Bhardwaj:** Investigation. **Amit Jaiswal:** Investigation. **Pranjal Chandra:** Conceptualization, Data curation, Formal analysis, Funding acquisition, Methodology, Project administration, Resources, Supervision, Validation, Visualization, Writing - original draft, Writing - review & editing.

Acknowledgement

This work is supported by research grant, project number BT/PR16634/NER/95/225/2015 awarded to Dr. Pranjal Chandra by Department of Biotechnology (DBT), Government of India. KM, BP acknowledges the Ph.D. research fellowship supported by IIT-Guwahati.

Appendix A. Supplementary data

Supplementary data to this article can be found online at https://doi.org/10.1016/j.bios.2019.111502.

References

Ahlawat, M., Sarkar, A., Roy, S., Jaiswal, A., 2019. ChemNanoMat 5 (5), 625–633.
Andén, N.-E., Magnusson, T., 1967. Acta Physiol. Scand. 69 (1-2), 87–94.
Baranwal, A., Chandra, P., 2018. Biosens. Bioelectron. 121, 137–152.
Barnett, N.W., Hindson, B.J., Lewis, S.W., 1998. Anal. Chim. Acta 362 (2), 131–139.
Burtis, C.A., Ashwood, E.R., Bruns, D.E., 2012. Tietz textbook of clinical chemistry and molecular diagnostics-e-book. Elsevier Health Sciences.
Camilleri, M., 2009. Curr. Opin. Endocrinol. Diabetes Obes. 16 (1), 53.
Carver, C.S., Johnson, S.L., Joormann, J., 2009. Curr. Dir. Psychol. Sci. 18 (4), 195–199.
Chandra, P., Tan, Y.N., Singh, S.P., 2017. Next Generation Point-Of-Care Biomedical Sensors Technologies for Cancer Diagnosis. Springer.
Chandra, P., 2016. Nanobiosensors for Personalized and Onsite Biomedical Diagnosis. IET, London.
Durairaj, S., Sidhureddy, B., Cirone, J., Chen, A., 2018. Appl. Sci. 8 (9), 1504.
Fayemi, O.E., Adekunle, A.S., Ebenso, E.E., 2017. Sens. Biosens. Res. 13, 17–27.
Feldman, J.M., 1986. Clin. Chem. 32 (5), 840.
Godoy-Reyes, T.M., Llopis-Lorente, A., Costero, A.M., Sancenón, F., Gaviña, P., Martínez-Máñez, R., 2018. Sens. Actuators B Chem. 258, 829–835.
Lacasse, J.R., Leo, J., 2005. PLoS Med. 2 (12), e392.
Mahato, K., Chandra, P., 2018. Biosens. Bioelectron. 128, 9–16.
Mahato, K., Maurya, P.K., Chandra, P., 2018. 3 Biotech 8 (3), 149.
Mahato, K., Srivastava, A., Chandra, P., 2017. Biosens. Bioelectron. 96, 246–259.
Maurer-Spurej, E., Dyker, K., Gahl, W.A., Devine, D.V., 2002. Br. J. Haematol. 116 (3), 604–611.
Moon, J.-M., Thapliyal, N., Hussain, K.K., Goyal, R.N., Shim, Y.-B., 2018. Biosens. Bioelectron. 102, 540–552.
Murugesan, A., Rani, M.R.S., Hampson, J., Zonjy, B., Lacuey, N., Faingold, C.L., Friedman, D., Devinsky, O., Sainju, R.K., Schuele, S., Diehl, B., Nei, M., Harper, R.M., Bateman, L.M., Richerson, G., Lhatoo, S.D., 2018. Epilepsia 59 (6), e91–e97.
Pallela, R., Chandra, P., Noh, H.-B., Shim, Y.-B., 2016. Biosens. Bioelectron. 85, 883–890.
Patel, B.A., Arundell, M., Parker, K.H., Yeoman, M.S., O'Hare, D., 2005. J. Chromatogr. B 818 (2), 269–276.
Plapp, F.V., 2019. Carcinoid Syndrome. ClinLabNavigator.
Priebe, M., Fromm, K.M., 2015. Chem. Eur J. 21 (10), 3854–3874.
Si, B., Song, E., 2018. Chemosensors 6 (1), 1.
Singh, P., König, T.A.F., Jaiswal, A., 2018. ACS Appl. Mater. Interfaces 10 (45), 39380–39390.
Singh, P., Roy, S., Jaiswal, A., 2017. J. Phys. Chem. C 121 (41), 22914–22925.
Šolínová, V., Žáková, L., Jiráček, J., Kašička, V., 2019. Anal. Chim. Acta 1052, 170–178.
Vural, P., Akgül, C., Canbaz, M., Yildirim, A., 1999. Turk. J. Med. Sci. 29 (2), 141–144.
Wu, K., Fei, J., Hu, S., 2003. Anal. Biochem. 318 (1), 100–106.
Yang, C., Denno, M.E., Pyakurel, P., Venton, B.J., 2015. Anal. Chim. Acta 887, 17–37.
Yılmaz, C., Taş, N.G., Kocadağlı, T., Gökmen, V., 2019. Food Chem. 272, 347–353.
Zestos, A.G., 2018. Int. J. Electrochem. 2018, 19.